

A-NeRF: Surface-free Human 3D Pose Refinement via Neural Rendering

SHIH-YANG SU, University of British Columbia

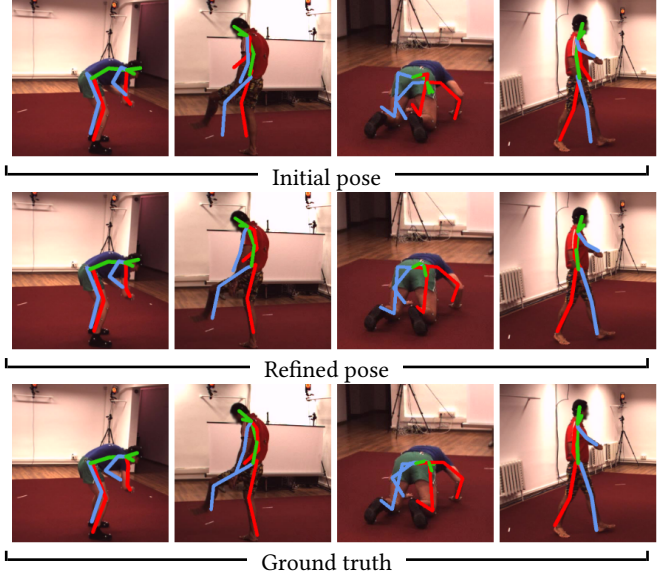
FRANK YU, University of British Columbia

MICHAEL ZOLLHOFER, Facebook Reality Labs Research

HELGE RHODIN, University of British Columbia



(a) Our human representation in unseen poses and novel views



(b) Pose refinement for real-image data

Fig. 1. Our A-NeRF test-time optimization for monocular 3D human pose estimation jointly learns a volumetric body model of the user that can be animated and works with diverse body shapes (left), while also refining the initial 3D skeleton pose estimate from a single or, if available, multiple views without tedious camera calibration (right). Underlying is a surface-free neural representation and skeleton-based embedding coupled with volumetric rendering. Faces in H3.6M images blurred for anonymity.

While deep learning has reshaped the classical motion capture pipeline, generative, analysis-by-synthesis elements are still in use to recover fine details if a high-quality 3D model of the user is available. Unfortunately, obtaining such a model for every user *a priori* is challenging, time-consuming, and limits the application scenarios. We propose a novel test-time optimization approach for monocular motion capture that learns a volumetric body model of the user in a self-supervised manner. To this end, our approach combines the advantages of neural radiance fields with an articulated skeleton representation. Our proposed skeleton embedding serves as a common reference that links constraints across time, thereby reducing the number of required camera views from traditionally dozens of calibrated cameras, down to a single uncalibrated one. As a starting point, we employ the output of an off-the-shelf model that predicts the 3D skeleton pose. The volumetric body shape and appearance is then learned from scratch, while jointly refining the initial pose estimate. Our approach is self-supervised and does not require any additional ground truth labels for appearance, pose, or 3D shape. We demonstrate that our novel combination of a discriminative pose estimation technique with surface-free analysis-by-synthesis outperforms purely discriminative monocular pose estimation approaches and generalizes well to multiple views.

1 INTRODUCTION

Human motion capture is an important research problem in computer graphics and computer vision with many applications ranging from character animation for computer games or movies to motion analysis for sports or medicine. Capturing the complex and highly articulated motion of human performances is an extremely challenging research problem, especially if only a monocular camera setup is available. One reason for this is the high level of depth ambiguity, i.e., there are multiple possible 3D scenes that project to the same 2D image.

Modern motion capture techniques combine the advantages of discriminative and generative techniques to obtain the highest quality results. First, a neural network-based 3D human pose estimation approach is employed to provide a coarse initial estimate of the human pose. These algorithms internalize a sophisticated pose prior and are thus able to counteract the depth ambiguity, but the obtained results might be noisy and do not perfectly re-project on top of the input image. Afterwards, generative approaches based on either a

high-quality 3D scan of the person [Habermann et al. 2019] or a parametric human body model [Alldieck et al. 2019a] are employed to refine the pose estimate. In this step, cues in the input image can be directly leveraged, e.g., additionally available silhouette masks or directly the color information. This allows the approach to better fit the model to the image than the purely discriminative approach. Although such combined techniques achieve unprecedented accuracy, their downside is that they require a shape body model or a personalized 3D scan of the person to be available *a priori*. Parametric 3D body models are not able to accurately model a particular user, especially in terms of clothing, since they are not part of the model and human appearances are diverse. A textured high-quality 3D scan provides the most accurate additional constraints, but it is challenging to acquire and limits the application scenarios.

We propose a surface-free neural rendering method for estimating a 3D body model and refining skeleton pose jointly, thereby alleviating the constraints and cost of template models, while maintaining the advantages of generative body models.

Recently, volumetric neural rendering techniques have shown very promising results for novel-view synthesis of static scenes. These surface-free approaches are able to represent arbitrary scenes by modeling the properties of every location in space based on its local radiance and opacity. Image formation is based on classical volumetric rendering techniques, such as ray marching and importance sampling for improved efficiency. One of the approaches that can handle small dynamic real-world scenes that have been observed by a multi-camera capture setups is Neural Volumes (NVs) [Lombardi et al. 2019]. NVs parameterize the scene based on a dense voxel grid of opacity and view-conditioned color that is regressed by an encoder-decoder network. NVs requires a dense multi-view camera setup for training and can only model small scenes at high resolution, due to the inherent cubic memory complexity of the underlying dense grid. One other approach that has obtained a lot of attention, is Neural Radiance Fields (NeRF) [Mildenhall et al. 2020] due to its stunning high quality results and the compactness of the learned scene representation. NeRF parameterizes the scene compactly using a Multi-layer Perceptron (MLP) as its scene representation that maps a 5D coordinate (position and direction) to the radiance and opacity at that position in space. However, NeRF only works for static scenes captured from dozens of calibrated camera positions. It is unclear how to extend this approach to dynamic scenes captured by a single uncalibrated camera, especially highly articulated human performances without a clear reference frame.

The question we answer in this paper is: Can we combine the advantages of volumetric rendering with analysis-by-synthesis (also called render-and-compare) to further improve monocular human pose estimation? We propose a novel test-time optimization approach for 3D human pose estimation that jointly learns a volumetric body model of the user to improve pose estimation accuracy that we term Articulated NeRF (A-NeRF). By initializing the pose estimate with an existing CNN-based pose estimation method, A-NeRF is applicable to as few as a single static camera and, if available, can integrate multi-view information from additional uncalibrated views to boost performance while keeping the capture setup simple.

The core technical novelty lies in our skeleton-relative embeddings. These encode positions and view-directions relative to the

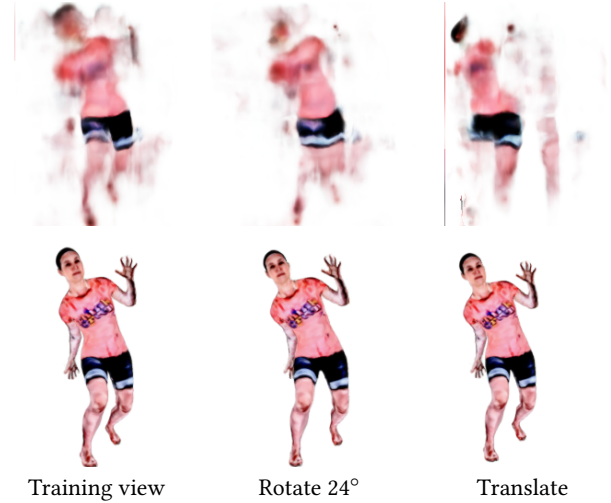


Fig. 2. Robustness and invariance. The original NeRF (top row) breaks when training on a diverse set of poses and further degrades when the poses are rotated or shifted. With our skeleton-relative encoding (bottom row), the geometry for the subject is consistent under rotation and translation.

bones of an articulated skeleton. Our relative pose embeddings have the advantage of being invariant to global translation and rotation of the person, thus allowing the network to better combine body shape and appearance constraints across the entire captured sequence (see Figure 2). In particular, a body part at frame k should look similar to k' if the pictured pose is similar, independent of the global position and rotation of the person in 3D space. More precisely, the introduced hierarchical skeleton structure links information from different frames even if a pose is only locally similar on a subset of body parts. Note, this does not include illumination changes due to the global motion of the person, thus we explicitly factor out this variation into a set of jointly learned low-dimensional appearance codes. Our strategy makes learning more feasible since it induces an inductive bias to the network, much like the translation invariance of 2D or 3D convolutions. Learning a NeRF model as a function of this embedding forces the underlying neural network to learn a representation that is consistent with the underlying body pose. The skeleton serves as a common reference frame linking all monocular observations across time, thereby alleviating the need for complicated multi-view capture setups.

In summary, our core technical contributions are:

- A novel volumetric analysis-by-synthesis approach for monocular 3D human pose refinement that jointly learns a volumetric body model and pose refinement of an initial 3D skeleton pose estimate in a self-supervised manner.
- Skeleton-relative embeddings that induce favorable inductive biases to scene representation MLPs.
- A multi-view extension that lets us integrate multiple uncalibrated camera views for an additional boost in performance.

We demonstrate that the test-time pose refinement improves on state-of-the-art approaches for monocular skeleton-based 3D pose reconstruction. Additional gains are possible by exploiting uncalibrated multi-view sequences. Moreover, we provide detailed

ablation studies that reveal the importance of the proposed skeleton embedding and the robustness of its hyperparameters. The learned body model is more accurate when using the proposed refinement and can readily be used for animation, appearance and motion transfer.

2 RELATED WORK

Our approach builds on prior work on motion capture and neural scene representations, which we discuss here with a focus on 3D representations for human modeling. For a detailed discussion of more general and image-based neural rendering we refer to [Tewari et al. 2020].

2.1 Human Modeling

Human modeling from images is an important research direction within computer vision and computer graphics. In the following, we discuss the pros and cons of existing approaches with a focus on the employed body representation, such as 3D point clouds, 3D skeletons, surface meshes, parametric shape models, voxel-based representations, and implicit surface models.

3D Joint Position Estimation. For many computer vision applications, such as action recognition and performance analysis in sports, it suffices to reconstruct motion as the 3D trajectories of the major human joints. Lifting-based approaches first estimate the 2D pose and then use a separate neural network to lift predictions to 3D based on a regressed depth value [Martinez et al. 2017]. Among these, our pose-relative encoding takes inspiration from Moreno-Noguer [2017], who showed that encoding 2D and 3D pose as the over-complete space of distances between all joint positions yields favorable invariances and relations. While lifting is light-weight and generalizes well, end-to-end reconstruction with CNNs still attains the highest accuracy [Li et al. 2020a; Xu et al. 2020]. However, pure positional information lacks information on the bone rotation and can lead to anatomically impossible poses.

Skeleton Motion Capture. Most computer graphics applications, such as animation and motion retargeting, require an articulated skeleton representation with fixed bone lengths that is parametrized by joint angles via forward kinematics. This representation can be obtained in a post process via inverse kinematics on the 3D joint locations predicted by the methods explained in the previous section, even in real-time [Mehta et al. 2017] and for groups of persons [Mehta et al. 2020]. However, strictly enforcing anatomical constraints comes at the expense of slightly less accurate reconstructions that do not perfectly reproject onto the input images. An alternative is to directly regress the joint angles of the skeleton [Shi et al. 2020; Zhou et al. 2016] and body proportions [Kocabas et al. 2020; Kolotouros et al. 2019]. While more accurate, single-shot, discriminative prediction is still prone to misalignment when overlayed onto the input image.

Surface Performance Capture. A common strategy for recovering surface detail is to roughly align a template mesh using one of the previous approaches and to refine its silhouette to match an image segmentation [Habermann et al. 2019; Xu et al. 2018]. The interior can be refined with shape-from-shading [Wu et al. 2011] or photometric terms [Robertini et al. 2016]. However, these approaches

require multiple views [Orts-Escalano et al. 2016] a laser scan, or other actor calibration steps with scripted motion [Alldieck et al. 2019a] and often depend on manual rigging [Xu et al. 2018] (association of vertices to skeleton bones via skinning weights). Our goal is to learn an actor model without a separate calibration step and for unconstrained actor motion.

Fitting Parametric Body Models. Parametric human body models [Balan et al. 2007; Choutas et al. 2020; Loper et al. 2015] enabled a large number of computer graphics applications, such as movie editing and reshaping [Jain et al. 2010]. They are learned from large collections of scans and fitted with a skeleton rig and constrain the space of plausible human shapes and motions in a low-dimensional space. This enables real-time reconstructions from single images [Bogo et al. 2016; Guan et al. 2009], alleviates manual rigging, and enables test-time optimization [Dong et al. 2020; Guler and Kokkinos 2019; Lassner et al. 2017] and weak-supervision when integrated in differentiable form [Liu et al. 2019] into the neural training process [Kanazawa et al. 2018; Kolotouros et al. 2019; Omran et al. 2018; Pavlakos et al. 2018; Tung et al. 2017]. The result are virtual, often animatable, characters for games or VR applications. Closest to our approach in this category is the model fitting and test-time refinement methods by [Zuffi et al. 2019] that textures and geometrically refines an untextured parametric quadruped model to zebra images and by [Xiang et al. 2019] that uses optical flow to refine human pose. Although similar in spirit, our surface-free neural body model and volumetric rendering is fundamentally different to their textured triangle mesh in a differentiable rasterization pipeline.

Hybrid approaches. Parametric models can be refined locally, e.g., in texture space predicting displacement maps [Alldieck et al. 2018a, 2019b]. These neural models are differentiable, enabling test-time optimization on silhouettes [Alldieck et al. 2019a, 2018b]. The learned offsets mitigate the constraint of classical parametric models that limit shapes by those in the training set. However, they require garment-specific handling of loose clothing such as skirts [Bhatnagar et al. 2019]; things that can not be modeled as an offset to pre-defined geometry.

From the rendering standpoint, A-NeRF bears close similarities with the volumetric body models and renderers by [Rhodin et al. 2016b, 2015], which refine human pose, shape, and appearance via differentiable ray-tracing in a multi-view camera setup. By defining the volumetric density as a sum of Gaussians, real-time reconstruction in egocentric perspective enabled immersive, real-time VR applications [Rhodin et al. 2016a]. However, the reconstructions have blurry appearance, two or more views are required, and an underlying parametric model limits generalization to specific subjects. Huang et al. [2020] uses a similar differentiable rendering on spherical primitives attached to a skeleton, but without optimizing the underlying pose. Our key differentiating factor is that our body model is surface-free and independent of parametric body models, alleviating their limitations.

Implicit Body Models. Implicit models describe the surface of a human as the level-set of a function, by a sum of simple functions, such as Gaussians [Stoll et al. 2011], or more recently by general purpose neural networks [He et al. 2020; Huang et al. 2020; Saito et al. 2019,

2020]. Most related to ours is NASA [Deng et al. 2019] that defines an implicit function as the minimum of individual implicit functions that are rigidly attached to the bones of a skeleton, each conditioned on the entire human pose to model dependencies and learned from 3D scans. By contrast, we learn a volumetric instead of a surface model, condition pose differently, and include appearance and rendering; all geared towards learning and refining human models from images.

2.2 Neural Scene Representations

A large number of recent work combine classical computer graphics techniques with a deep neural scene representations. We draw upon these general purpose representations for our human model. Many classical computer graphics representations have been used as the basis for neural rendering approaches, such as meshes [Lombardi et al. 2018; Thies et al. 2019], point clouds [Aliev et al. 2019; Meshray et al. 2019; Wiles et al. 2020], a set of spheres [Lassner and Zollhöfer 2020], and dense volumetric grids [Lombardi et al. 2019; Sitzmann et al. 2019a]. Recently, volumetric neural representations have been widely applied, due to their generality and the fact that they have shown very promising results. These representations are based either on a dense volumetric grid or an MLP.

Dense Volumetric Grids. Deep Voxels [Sitzmann et al. 2019a] employs a coarse volumetric grid of learned features as the 3D scene representation. The features can be reprojected to novel views to condition a U-Net based neural rendering network that regresses the final color output. Deep Voxels is limited to novel view synthesis for static scenes. Neural Volumes (NVs) [Lombardi et al. 2019] learn to parameterize a dynamic object based on an encoder-decoder network that regresses a volumetric grid of opacity and view-conditioned color. Image formation is based on a differentiable raymarching approach that is inspired by additive alpha blending. NVs require a dense multi-view camera setup for training. One limitation of all approaches that are based on a dense voxel grid is that they can only handle scenes with a small spatial extent due to their cubic memory requirements.

MLP-based Volumetric Approaches. Neural Radiance Fields (NeRF) parameterize a static scene compactly using an MLP-based scene representation [Mildenhall et al. 2020]. One important component is the positional encoding of the query point coordinates [Mildenhall et al. 2020; Tancik et al. 2020] that enables the approach to represent high frequency detail. Sitzmann et al. [2019b] proposed Scene Representation Networks (SRNs) that assign a feature to every point in 3D space based on an MLP and also jointly learns a differentiable sphere marcher for image generation. Liu et al. [2020] proposed Neural Sparse Voxel Fields (NSVF) that combines an Octree acceleration structure with a latent-conditioned MLP. The Octree enables the approach to prune empty space and thus can speed up rendering of the scene representation. Currently, all these approaches are restricted to static scenes.

Non-peer Reviewed Works. There is a large number of recent extensions to MLP-based neural scene representations: These approaches focus on general improvements [Tancik et al. 2020; Zhang et al. 2020], in-the-wild data [Martin-Brualla et al. 2020], generalization

aspects [Gao et al. 2020; Schwarz et al. 2020; Trevithick and Yang 2020; Yu et al. 2020], and extending the approach to the dynamic setting [Du et al. 2020; Gafni et al. 2020; Li et al. 2020b; Park et al. 2020; Peng et al. 2020; Pumarola et al. 2020; Tretschk et al. 2020; Xian et al. 2020]. These works are not yet peer-reviewed and only available as technical reports via arXiv. Thus, they are not considered prior art.

3 METHOD

We follow the classical analysis-by-synthesis approach of refining an initial human pose estimate θ_k by rendering the current model configuration and iteratively optimizing the pose to minimize the difference between a real image I_k and the rendering (also called render-and-compare). This optimization is done *at test time* over the video or collection of images, $\{I_k\}_{k=1}^n$, that should be reconstructed. This is a practical setting since we do not require any 3D annotation or camera calibration. Figure 3 provides an overview of our method.

Unique to our approach is that we learn the human body shape and appearance during optimization without relying on restrictive template scans or parametric shape models. We dub this model Articulated Neural Radiance Field (A-NeRF). We explain in the following how the refinement is initialized with an existing discriminative model (Section 3.1) and how we realize the joint estimation of shape, appearance, and pose (Section 3.2) via a combination of classical volumetric rendering, neural scene representation (Section 3.3), and a novel embedding into the kinematic chain of an articulated skeleton (Section 3.4). The training of the underlying neural network is explained in Section 3.5 and further extensions in Section 3.6.

3.1 Skeleton Pose Initialization

Given a set of n images $\{I_k\}_{k=1}^n$ of a single human subject, we utilize SPIN [Kolotouros et al. 2019], a the state-of-the-art 3D pose and shape estimation method. Importantly for us, it yields not only human joint positions, but also approximate camera parameters, joint angles, and thereby skeleton bone orientation, which we use to initialize the parameters θ_k of an articulated skeleton and camera intrinsics K_k for every input frame k . SPIN is a feed-forward neural network that has been trained on a combination of studio recordings and in-the-wild images.

Our skeleton representation follows that of SMPL [Loper et al. 2015], but without the associated parametric surface model. The skeleton structure is defined in a restpose of $m = 24$ 3D joint locations $\{a_i\}_{i=1}^m$, with the root at 0 . In the subsequent paragraphs, we use the subscript (k, i) to indicate that a variable is related to the i -th joint of frame k . The skeleton pose that we deem to reconstruct, $\theta_k = [\omega_{k,0}, \dots, \omega_{k,24}]$, consists of the relative rotation of 24 joints, $\omega_{k,i}$, in either axis-angle form ($\omega_{k,i} \in \mathbb{R}^3$) or the recently proposed overparametrized representation of [Zhou et al. 2019] ($\omega_{k,i} \in \mathbb{R}^6$) and $\omega_{k,0} \in \mathbb{R}^3$ the global root position. Every joint determines the relative orientation of a bone to its parents. We refer to the coordinate system spanned by the joint rotation axis $\omega_{k,i}$ and vector between i and its parent as local bone coordinates. The 3D world coordinates $q \in \mathbb{R}^3$ of a point $p_{k,i} \in \mathbb{R}^3$ in the i -th local bone coordinates is then computed with forward kinematics using

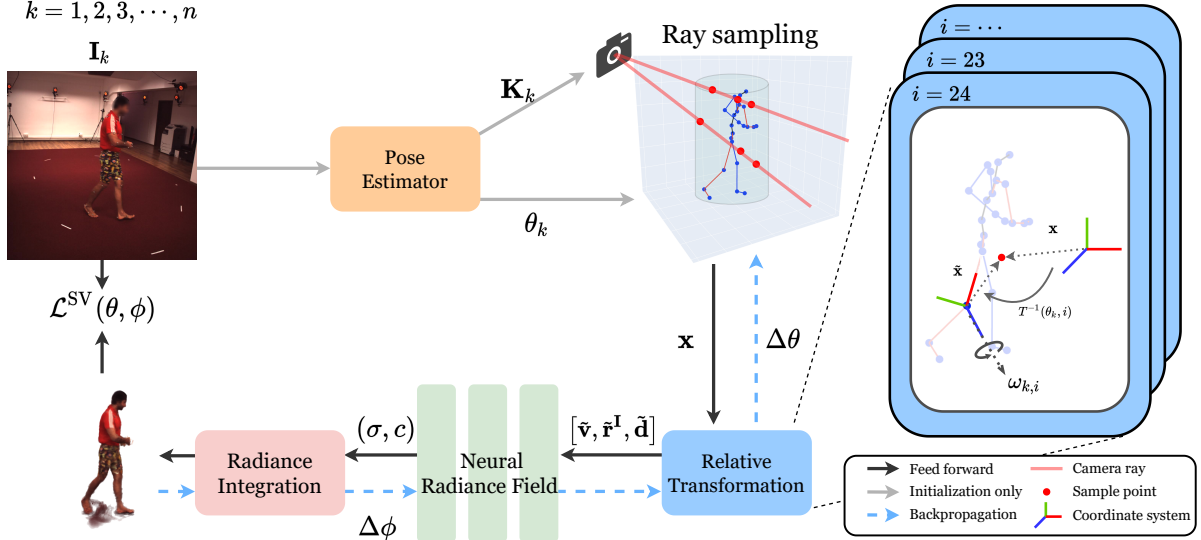


Fig. 3. **Overview.** Our human body model (bottom left) is learned using a photometric reconstruction loss \mathcal{L}^{SV} . First, the skeleton pose is initialized with an off-the-shelf pose estimator (gray arrows). Second, this pose is refined via analysis-by-synthesis using volumetric rendering (the step after NeRF) of a neural radiance field (green). Key is a skeleton-relative embedding that links the neural encoding with skeleton pose and enables their joint learning (blue). Faces in H3.6M images blurred for anonymity.

homogeneous coordinates,

$$\begin{bmatrix} \mathbf{q} \\ 1 \end{bmatrix} = T(\theta_k, i) \begin{bmatrix} \mathbf{p} \\ 1 \end{bmatrix}, \quad (1)$$

with the 4×4 local-to-world transformation matrix

$$T(\theta_k, i) = \prod_{j \in A(i)} \begin{bmatrix} \mathbf{R}(\omega_{k,j}) & \mathbf{a}_j \\ \mathbf{0} & 1 \end{bmatrix}, \quad (2)$$

$\mathbf{0} = [0, 0, 0]$, $A(i)$ is the ordered set of the joint ancestors of i , and $\mathbf{a}_i \in \mathbb{R}^3$ the joint location of i at the rest pose. Since SPIN predicts $\mathbf{a}_i \in \mathbb{R}^3$ for every image, we average the rest pose over all k to obtain consistent bone length estimates. The rotation matrix $\mathbf{R}(\omega_{k,j})$ is inferred from the axis angle representation via Rodrigues formula or by [Zhou et al. 2019] in the 6D case.

3.2 A-NeRF—Setting and Pose Refinement Objective

Our goal is to learn a volumetric body model parametrized by ϕ and to optimize the agreement of its rendering $P_\phi(\theta_k)$ on the set of images $\{I_k\}_{k=1}^n$ with respect to the underlying skeleton pose θ_k . Formally, we write the joint modeling and reconstruction objective

$$\mathcal{L}^{\text{SV}}(\theta, \phi) = \sum_k d(P_\phi(\theta_k), I_k) + \lambda d(\theta_k, \hat{\theta}_k), \quad (3)$$

where ϕ are the parameters of a neural network defining density and radiance of a volume, P_ϕ is a classical volumetric renderer that ray casts the neural volume, $\hat{\theta}_k$ is the initial pose estimate from SPIN, λ is a hyperparameter that controls the regularization strength, and d is a distance function, such as the l_1 distance.

This objective is optimized using stochastic gradient descent. In other words, we jointly train the neural network parameters ϕ that define how the body model is rendered given pose θ_k as well as refine the pose θ_k such that the same model ϕ can explain each

image I_k . The last term $\lambda d(\theta_k, \hat{\theta}_k)$ controls the amount of changes to apply to the initial estimate $\hat{\theta}_k$. How pose and model are linked is explained in the following sections.

Assumptions. We assume that the images I_k stem from one or multiple videos of the same person captured with static cameras. In the most general case, the input is a monocular video but we also provide an extension that imposes multi-view constraints if multi-view footage is available. We distinguish the single-view and multi-view case with \mathcal{L}^{SV} and \mathcal{L}^{MV} , respectively. Notably, we do not require intrinsic or extrinsic camera calibrations in either of these settings. This is different from many structure-from-motion approaches, which explicitly require camera motion with a strong translation component to calibrate; impractical for casual recordings. This uncalibrated setup drastically eases setup time compared to existing solutions that operate in the same accuracy range.

Most importantly, the neural body model ϕ is learned from scratch, no parametric actor model nor separate model calibration step is required, which additionally eases its application. The steps required to attain this level of automation are explained in the following.

3.3 Volumetric Rendering with Neural Radiance Fields

Our rendering model follows that of NeRF [Mildenhall et al. 2020], with only minor additions to the importance sampling that improve the effectiveness by exploiting the estimated initial skeletal pose θ .

NeRF stores the density σ and radiance \mathbf{c} of a 3D point \mathbf{x} in view direction \mathbf{d} using a 10-layer fully-connected neural network $(\sigma, \mathbf{c}) = F_\phi(\mathbf{x}, \mathbf{d})$ with 946500-dimensional parameters ϕ . Similar to classical frequency-space embeddings of volumetric data, this yields

a compact parametric representation of the scene that can be ray-cast by sampling \mathbf{x} along the view direction \mathbf{d} . NeRF attained a breakthrough by using positional encoding, the projection of the query 3D position onto a high number of spatial sine and cosine waves of varying wavelengths. Conditioning on this high-dimensional space encourages the learning of low and high frequency features.

This neural density and radiance field is then formed into an image by ray casting. Each ray emitted from the camera is first sampled at 64 points and F_ϕ is evaluated at each. The samples together form a piece-wise constant probability density function (PDF) that is integrated using the Beer-Lambert law. A pixel at coordinate (u, v) is rendered as

$$P_\phi(u, v) = \sum_i T(x_i)(1 - \exp(-\sigma(x_i)\delta(x_i)))\mathbf{c}(x_i), \text{ with} \quad (4)$$

$$T(x_i) = \exp\left(-\sum_{j=1}^{i-1} \sigma(x_i)\delta(x_j)\right), \quad (5)$$

and x_i the sample points, $\delta(x_i)$ the distance between x_i and x_{i+1} , and $T(x_i)$ the accumulated transmittance for the ray traveling from the near plane to x_i .

At training time, the neural network parameters ϕ are optimized by minimizing the distance between the rendered pixel color $P_\phi(u, v)$ and the true image color $\mathbf{I}(u, v)$ at pixel coordinate (u, v) . In essence, the image formation function, which is differentiable, takes the role of a fixed-pipeline neural network layer that connects to the underlying NeRF network. It facilitates end-to-end training of the network parameters ϕ , which subsequently encode the radiance and density of the entire scene and can be rendered from novel views by changing the virtual camera (view direction \mathbf{d}).

We follow the original work in using a coarse-to-fine training strategy. A second neural network F'_ϕ is learned by sampling 16 additional samples from the piecewise-constant PDF inferred from the 64 initial samples and repeating the above rendering with the 64+16 locations. Since both neural networks have the same structure and function and are trained and evaluated in sequence, we make no distinction in the following.

However, the original NeRF formulation was designed to reconstruct a single static scene from a massive number of calibrated views, which is not applicable to our setting of a moving person unless captured in a camera dome. Straight-forward extensions that we tried, such as conditioning F_ϕ on the frame or initial pose estimate θ fail in that the neural network either memorizes all the possible mappings of $(\sigma, \mathbf{c}) \leftarrow (\theta, \mathbf{x}, \mathbf{d})$ from a small training set and degrades into fog-like artifacts when the number of training poses increases. It generalizes poorly not just to unseen human poses, but also to shifted or rotated training poses, as shown in Figure 2 and Section 4.2.

3.4 A-NeRF—Pose-Relative Embedding

Motivated by the observation that the positional encoding in terms of frequency components in NeRF was a game changer, we derived a novel embedding that is tailored for articulated human motion. The idea is to define the model density and radiance relative to the rigid bones of the skeleton instead of explicitly conditioning on

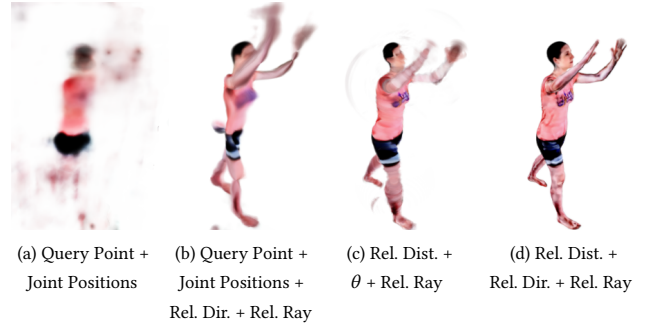


Fig. 4. Encoding ablation study on a novel view. (a) Directly applying positional encoding on the concatenation of query point \mathbf{x} as in NeRF is unsuitable for learning pose-dependent models, even when conditioning on the skeleton joint locations. Also when encoding only the directional information (b) or distances and view-ray direction relatively (c) artifacts remain. (d) Our Pose-relative representation drastically improves the quality of the articulated human representation.

skeleton pose. Although not providing additional information to the neural radiance field, this creates an implicit bias that encourages the network to store only that information in relation to bone j that is influenced by j . Embedding information of other joints would not be consistent under relative pose changes; thereby, discouraging dependencies due to the increased complexity of relations.

In the following, we introduce five skeleton-relative embedding variants that replace the positional encoding in Euclidean space explained in the previous section. Each of them first maps the 3D query point \mathbf{x} via the inverse of the bone-to-world transformation $T(\theta_k, i)$ explained in Section 3.1. Formally we write

$$\begin{bmatrix} \tilde{\mathbf{x}}_{k,i} \\ 1 \end{bmatrix} = T^{-1}(\theta_k, i) \begin{bmatrix} \mathbf{x} \\ 1 \end{bmatrix}. \quad (6)$$

An overview of all embeddings is given in Figure 4.

Relative Positional (Rel. Pos.) encoding. The query point \mathbf{x} is mapped to all bones of the skeleton with Equation 6. Because we perform positional encoding afterwards as in the original NeRF, this blows up the already massive positional encoding space by a factor of the number of joints (for us 24), drastically increasing the memory footprint.

To this end, we propose the following alternatives. Two for encoding the query position and two for the view direction.

Relative Distance (Rel. Dist.) encoding. Given θ_k , we calculate the l_2 distance from the 3D query point \mathbf{x} to joint i by

$$\tilde{\mathbf{v}}_{k,i} = \|\tilde{\mathbf{x}}_{k,i}\|_2. \quad (7)$$

Recall, $\tilde{\mathbf{x}}_{k,i}$ is \mathbf{x} in the local coordinate of joint i . Storing only the distance reduces input parameters by a factor of three.

Relative Direction (Rel. Dir.) encoding. Since the distance maps many 3D points to the same scalar, we additionally obtain the direction vector to capture the orientation information of \mathbf{x} by

$$\tilde{\mathbf{r}}_k^i = \frac{\tilde{\mathbf{x}}_{k,i}}{\|\tilde{\mathbf{x}}_{k,i}\|_2}. \quad (8)$$

We do not apply positional encoding on this direction encoding, which dramatically saves network capacity.

Relative Ray Direction (Rel. Ray.) encoding. NeRF builds upon a radiance field that is a function of the position and view direction. To encode the view direction, we transform \mathbf{d} to obtain the relative view-ray direction $\tilde{\mathbf{d}}$ by applying the rotational part of the bone-to-world transformation $T(\theta_k, i)$,

$$\tilde{\mathbf{d}} = [T^{-1}(\theta_k, i)]_{3 \times 3} \mathbf{d}, \quad (9)$$

with $[T^{-1}(\theta_k, i)]_{3 \times 3}$ the top-left 3×3 submatrix.

Relative Ray Angle (Ray. Angl.) encoding. The other view-direction encoding we explore is the angle between the ray \mathbf{d} and the vector \mathbf{u} from query point to joint origin,

$$\mathbf{d}' = \text{arc cos}(\mathbf{d} \bullet \mathbf{u}), \quad (10)$$

with \bullet the dot product. As the distance encoding for position, this encoding has the advantage of being one-dimensional.

These relative embeddings have the advantage of being invariant to global shift and rotation of the person and preserve the piece-wise rigidity of articulated motion while still allowing for pose-dependent deformation. The handling of view-dependent illumination effects is explained in the extensions section (Section 3.6).

3.5 A-NeRF—Pose-Relative Rendering and Learning

With our relative skeleton embeddings introduced, we now turn to defining our Articulated NeRF Rendering model that is tailored to modeling human shape and appearance and lends itself for pose refinement of the underlying skeleton.

In a first step, we leave the NeRF model as is and only change the input to the neural network that encodes the radiance field used for volumetric rendering. We will expand on further extensions in the subsequent section. Samples along each view ray are taken as before (see Section 3.3), however, now each query point is mapped to each of the $n = 24$ bone coordinate systems and projected to the previously introduced encodings. This yields vectors $\tilde{\mathbf{v}} = [\tilde{\mathbf{v}}_{k,1}, \dots, \tilde{\mathbf{v}}_{k,24}]$, $\tilde{\mathbf{r}} = [\tilde{\mathbf{r}}_{k,1}, \dots, \tilde{\mathbf{r}}_{k,24}]$ and $\tilde{\mathbf{d}} = [\tilde{\mathbf{d}}_{k,1}, \dots, \tilde{\mathbf{d}}_{k,24}]$, that are fed into the neural radiance field function

$$(\sigma, \mathbf{c}) = F_\phi(\tilde{\mathbf{v}}, \tilde{\mathbf{r}}, \tilde{\mathbf{d}}). \quad (11)$$

Image formation (Eq. 5) takes in the output of this re-parametrized NeRF but remains unchanged otherwise.

The effect is that density and radiance values are now stored relative to the skeleton parametrized by θ . Changing the skeleton parameters changes the local bone coordinate systems and therefore the density and radiance with them—like a manually rigged character would behave. This conditioning on pose allows us to optimize \mathcal{L}^{SV} , our objective (Eq. 3), jointly with respect to pose θ and neural network weights ϕ that define the radiance field.

It is a-priori unclear whether this joint optimization can succeed, in fact, our initial experiments on conditioning NeRF on pose explicitly did not. The employed neural network is a general function approximator that has the degrees of freedom to compensate to give the same output for two different configurations of θ . Nevertheless, our experiments show that our complete method can jointly refined pose from an off-the-shelf pose estimate. The learned model is not

only consistent and visually accurate but better matches the ground truth 3D pose.

We believe that our skeleton-relative encodings make learning feasible because they induce an implicit bias to the learning of the MLP, much like the invariance of convolutions, which helps CNNs to learn from images.

Relation to existing pose embeddings. An alternative would be to define the NeRF field in a reference pose and to map query points to this template. While this works well for points on or close to a surface [Huang et al. 2020; Taylor et al. 2012] and small deformation fields [Park et al. 2020], it is ill-posed for articulated motion. For instance, when left and right hand are close a nearby query point can not be uniquely attributed to the left or right side.

3.6 Extensions

We propose several extensions that make Articulated NeRF computationally tractable and more accurate.

Sparse sampling and gradient accumulation. At training time, we form a batch of rays by randomly sampling 2048 rays from all available images. Therefore, not every frame will be optimized in every iteration. Moreover, every frame that is included may only be sampled with a few rays. As a result, optimizing the θ at every iteration is prone to noise in the stochastic gradient estimate. To counteract, we accumulate the gradient update $\Delta\theta$ for 50 iterations before updating. Without this, pose refinement diverged in our experiments.

Background handling. In addition, to make our network focus on learning the subject’s representation, we provide the renderer with the background image B obtained as the median pixel value over all images taken from the same camera, exploiting the constant background assumption. Let $a(x_i) = T(x_i)(1 - \exp(-\sigma(x_i)\delta(x_i)))$, the render outputs at (u, v) becomes

$$P_\phi(u, v) = \left(1 - \sum_i a(x_i)\right) B(u, v) + \sum_i a(x_i) \mathbf{c}(x_i), \quad (12)$$

with the background filling that fraction of light that passes through the entire volume.

Sampling optimization. To further increase the sampling efficiency, we define a cylinder surrounding the initial skeleton pose estimate and sample points along the ray segment that lies inside. This is sketched in Figure 3. Moreover, we use the background estimate to segment the person and only sample rays inside. Because this estimate is uncertain, we dilate the initial segmentation by 3 pixels.

Positional Encoding with Cutoff. To capture the high frequency details from the training images $\{\mathbf{I}_k\}_{k=1}^n$, prior works incorporate periodic activation functions [Sitzmann et al. 2020] in their neural networks, or adding high frequency input components [Mildenhall et al. 2020; Tancik et al. 2020]. We follow the latter approach in our work. Specifically, we adopt a weighted version of positional

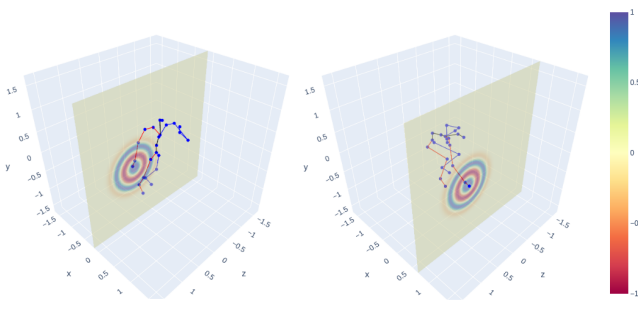


Fig. 5. Cutoff positional encoding relative to the right hand. We visualize two slices of the world coordinates, and the respective encoded values for the right hand joint in two different 3D poses. The encoded values are reduced to 0 for points that are too far away, so that they do not affect the final representation for the right hand.

encoding [Mildenhall et al. 2020; Vaswani et al. 2017]

$$\gamma(p, w) = w \left[p, \sin(2^0 \pi p), \cos(2^0 \pi p), \dots, \sin(2^{L-1} \pi p), \cos(2^{L-1} \pi p) \right], \quad (13)$$

where L is the number of frequency components, and w is the weighting factor. We calculate w as a per-joint weighting factor that depends on the distance $\tilde{v}_{k,i}$,

$$w_{k,i} = \begin{cases} 1, & \text{if } \tilde{v}_{k,i} \leq t \\ \exp\left(-\frac{1}{2s^2}(\tilde{v}_{k,i} - t)^2\right), & \text{otherwise.} \end{cases} \quad (14)$$

Here, t denotes a cutoff threshold, and s is a hyperparameter controlling how fast the Gaussian weight should be reduced to 0 as $\tilde{v}_{k,i}$ increases. We apply γ on the relative distance $\tilde{v}_{k,i}$ and view direction $\tilde{d}_{k,i}$ of all joints i such that

$$\tilde{v} = [\gamma(\tilde{v}_{k,1}, w_{k,1}), \dots, \gamma(\tilde{v}_{k,24}, w_{k,24})], \quad (15)$$

$$\tilde{d} = [\gamma(\tilde{d}_{k,1}, w_{k,1}), \dots, \gamma(\tilde{d}_{k,24}, w_{k,24})]. \quad (16)$$

The intuition behind this weighted positional encoding is that if the joint i is far away from x (i.e., has large $\tilde{v}_{k,i}$), its input encoding should have less influence on the output. Our empirical results show that the proposed encoding helps reduce noise in the background (Section 4.2).

Appearance codes. Illumination effects such as shadows and shading depend on the view direction in relation to the light position in world coordinates. We encode the former relative to the skeleton, which however is invariant to global position. Following concurrent work on handling illumination changes [Martin-Brualla et al. 2020], we add a 16-dimensional appearance code to the second last layer of the NeRF network F_ϕ . It is individually stored and optimized for every frame. Due to its position at the end of the network and its low dimensionality, it helps learning these global effects while not deteriorating the benefits of the relative encoding.

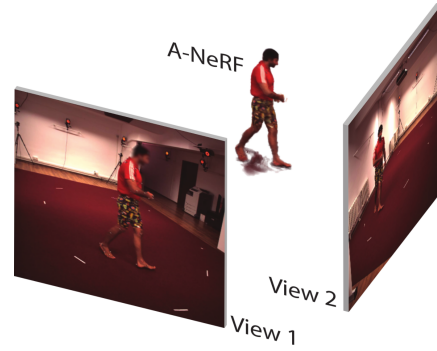


Fig. 6. Multi-view setup. Our A-NeRF learning and test-time pose refinement method naturally generalizes to multiple views. For every frame, a single view-consistent neural radiance field (center) as well as underlying 3D skeleton pose is reconstructed. The camera pose is estimated and refined for every frame and view automatically. Faces in H3.6M images blurred for anonymity.

Multi-view constraints. We can further incorporate a multi-view constraint to improve pose refinement when the motion is captured from multiple cameras. Figure 6 shows the two camera case that is most practical. For initializing θ_k , we average the individual joint rotation estimates from all V views $v \in [1, \dots, V]$. Since rotations are relative to the parent and root, this works without calibrating the cameras. Only the global position and orientation remains specific to view v . To this end, we extend our single-view notation with subscripts, position $\omega_{k,1}^{(v)}$ and orientation $\omega_{k,2}^{(v)}$ are estimated relative to camera v .

For refinement, we extend the single view objective Eq. 3 to make θ_k view-consistent. With slight abuse of notation we write,

$$\mathcal{L}^{\text{MV}}(\theta, \phi) = \sum_c \sum_k d(P_\phi(\theta_k, \omega_{k,0}^{(v)}, \omega_{k,1}^{(v)}, \mathbf{K}^{(v)}), \mathbf{I}_k^{(v)}) + \lambda d(\theta_k, \hat{\theta}_k), \quad (17)$$

with θ_k shared across all views v , except for the global skeleton position, $\omega_{k,0}^{(v)}$, and global orientation, $\omega_{k,1}^{(v)}$, which are estimated independently per camera view v since the relative camera position and orientation is unknown in our setting.

3.6.1 Implementation details. We train our A-NeRF for a total of 500k iterations: During the first 100k, we jointly update A-NeRF weights ϕ and refine pose estimates θ using the l_1 distance. We then stop optimizing θ , and continue to train the A-NeRF model for improved visual fidelity additional 400k iterations using the l_2 distance. We use Adam optimizer [Kingma and Ba 2015], and keep separate step sizes for A-NeRF and pose refinement. For A-NeRF, we start with step size 0.0005 and exponentially decay it to 0.00005. For pose refinement, we use a fixed step size of 0.001 throughout the joint optimization process, and set the regularization parameter $\lambda = 2$, and the cutoff threshold $t = 500\text{mm}$. The training is done on 1 Nvidia Tesla V100 32GB GPU, which takes approximately 60-70 hours. It takes around 8 seconds to render one $512 \times 512 \times 3$ image.

4 EVALUATION

We perform a large number of experiments on real as well as synthetic data. The synthetic experiments allow us to vary independent factors of variation and to have perfect ground truth. The evaluation on established benchmarks with real persons and images shows the generality of the approach and quantifies the improvements brought about by our contributions compared to the state-of-the-art approaches. Computer graphics applications of novel-view synthesis and retargeting are shown in the subsequent applications section.

4.1 State-of-the-art Pose Estimation

Human 3.6 M Benchmark Dataset. This dataset [Catalin Ionescu 2011; Ionescu et al. 2014] is the most widely used benchmark for single and multi-view human motion capture. Human3.6M features 3.6 million images captured from four cameras with varying position, five training subjects, two validation subjects, and accurate, marker-based 3D pose ground truth. We follow the widely used train/test split from [Nibali et al. 2019], subsampling the test videos at every 64th frame to reduce the dataset size from millions to thousands without compromising expressiveness. The test set features two subjects (S9 and S11) doing 14 different actions with two iterations each, their respective number of images to optimize is 5012 and 3712.

Metric. We report the MPJPE metric, the Euclidean distance between predicted and ground truth joint position averaged over all frames and joints of the test set. We utilize the PA-MPJPE variant that performs Procrustes alignment between prediction and ground truth. This alignment in scale and orientation is essential for comparing approaches that do not assume knowledge of the ground truth calibration and are, hence, ill-posed to the factors that the alignment removes.

Test-time Optimization. As explained in section Section 3.4, pose is initialized by applying SPIN on all test images individually. SPIN was trained on the Human3.6M training set among others. This initial estimate is then jointly refined with the learning of the A-NeRF model, for 100k iterations on all test images using Equation 3, without assuming any additional knowledge of the camera or 3D pose. In the machine learning literature, this is sometimes called transductive learning.

Comparison to Single-View Approaches. Table 1 categorizes 3D pose estimation approaches in four categories and compares within each. The single-view approaches that predict 3D joint position but not skeleton pose play in an individual class because not enforcing skeleton constraints allows for poses that have a low MPJPE but are unrealistic. For instance, the center between two possible modes with shrunk bone length, violating the constant bone-length assumption of those using skeletons. The most accurate 3D joint position estimation methods attain a PA-MPJPE of 39.0.

The best existing methods for predicting skeleton pose are VIBE with a PA-MPJPE of 41.4 and SPIN with a PA-MPJPE of 41.9 on the described protocol. Our test-time optimization improves upon SPIN by 3 % to 40.6, thereby improving on the state-of-the-art methods in skeleton pose prediction. Note that improvements in mm may

Table 1. Quantitative evaluation on Human3.6M [Ionescu et al. 2014]. Single-view 3D joint position methods obtain the highest accuracies. Our test-time optimization yields skeleton pose, which is slightly harder due to the kinematic constraints, and improves upon the SPIN and VIBE baselines. Additional gains are possible in the uncalibrated multi-view setup, with accuracies approaching that of the calibrated related work using all four cameras.

Method	PA-MPJPE↓
Single view, 3D joint positions:	
Pavlakos et al. [2017]	51.9
XNect [Mehta et al. 2020] (before skeleton fit)	48.5
Martinez et al. [2017]	47.7
Nibali et al. [2019]	39.0
Single view, 3D skeleton:	
MotioNet [Shi et al. 2020]	54.6
HoloPose [Guler and Kokkinos 2019]	46.5
SPIN [Kolotouros et al. 2019])	41.9
VIBE [Kocabas et al. 2020])	41.4
Ours (single-view)	40.6
Multi-view, unknown camera, 3D skeleton:	
SPIN-multiview (2 views)	38.2
Ours (2 views)	34.1
SPIN-multiview (4 views)	34.0
Ours (4 views)	30.6
Multi-view, known camera, 3D joint positions:	
Tome et al. [2018] (4 views)	44.6
Iskakov et al. [2019] (4 views)	20.8

appear marginal, but the dataset is nearly saturated with the most recent methods fighting for the last mm of improvement.

Comparison to Multi-view Approaches. Our approach naturally extends to multi-view inference, as introduced in Section 3.6. The lower half of Table 1 shows that our multi-view refinement improves over all single view approaches and outperforms simple baselines such as averaging pose estimates from the off-the-shelf SPIN pose estimators across views (SPIN-multiview). These improvements are consistent across two and four views, with four views being more accurate as expected.

We can not compete with approaches that utilize exact knowledge of the camera location, orientation, and intrinsic calibration. These boil down to detecting 2D body parts in each view and triangulating the 3D pose. This strategy, however, does not translate to our more general case where cameras are not manually calibrated. The methods listed in this category therefore only serve as a lower bound to the accuracy uncalibrated approaches may attain.

4.2 Ablation Studies

Synthetic Test Bench (SURREAL). To generate synthetic data of animated human performances, we employ the models of the SURREAL dataset [Varol et al. 2017] animated with motions from the CMU Graphics Lab Motion Capture Database¹. We build a training set of 10,800 frames by selecting 20 motion clips from the CMU MoCap

¹<http://mocap.cs.cmu.edu>

Table 2. Monocular vs. multi-view reconstruction. The PSNR and SSIM scores show that our model can learn as well from a single view as from multiple ones. Adding more and diverse poses to the training is more important than additional views.

#views	#poses	#imgs	PSNR ↑	SSIM ↑
1	1200	1200	24.02	0.9315
3	400	1200	23.76	0.9306
9	134	1206	23.52	0.9275
3	1200	3600	24.17	0.9360
9	1200	10800	24.39	0.9378

Table 3. Positional encoding trade-off. Encoding world coordinates does not succeed on motions and has a large memory consumption. Encoding positions relative to the skeleton works yet has also high dimensionality. Our full model that combines distance and direction performs well in both aspects.

Position Rep.	Direction Rep.	PSNR ↑	SSIM ↑	#dim for each Rep.
World Pos. + Joint Positions	Ray Ang.	1.95	0.1024	1080 + 72 + 216
World Pos. + Joint Positions	Rel. Ray	14.40	0.7585	1080 + 72 + 648
Rel. Pos.	Ray Ang.	23.62	0.9169	1080 + 216
Rel. Pos.	Rel. Ray	23.54	0.9177	1080 + 648
Rel. Dist. + Rel. Dir	Ray Ang.	23.33	0.9178	360 + 72 + 216
Rel. Dist. + Rel. Dir (our model w/o cutoff)	Rel. Ray	24.12	0.9228	360 + 72 + 648

dataset, 60 frames long each, and is captured by nine virtual cameras. We further create a evaluation set of 5 motion clips, including extreme motions like a back-flip, cart-wheel, and capoeira, with nine virtual cameras that are at new positions and angles.

Metrics. We measure image quality on a novel view of a pose unseen during optimization by comparing the dataset image with the rendering of A-NeRF, using the peak signal to noise ratio (PSNR) and structure similarity index (SSIM) [Wang et al. 2004]. The latter computes a contrast normalized similarity score between rendering and reference image.

Monocular vs. Multi-view quality. Surprisingly, the visual fidelity of our model trained on a single is nearly as good as trained on three or more views. Table 2 lists the PSNR and SSIM for 1, 3, and 9 views and different number of poses for each. The difference between using a single or multiple views is only 1% PSNR for 1200 poses. It is more important to have diverse poses rather than multiple synchronized views, as evidenced by the comparison of using the same number of images, where the monocular one scores higher by using only one camera but longer sequences. Multiple views are only beneficial for disambiguating depth ambiguities for 3D reconstruction, as explained in the previous section, but these have little influence on the learned appearance. All following ablation studies are performed with nine views.

Impact of Query Position Encoding. The neural radiance field is position and direction-dependent. We therefore analyze the effect of encoding each quantity individually. Table 3 shows that straightforwardly extending the original NeRF [Mildenhall et al. 2020] to learning a neural radiance field in world coordinates and conditioning on human pose (3D joint positions) yields low quality (PSNR <

Table 4. Distance-based positional encoding is compact (360 dim) but insufficient (lower PSNR and SSIM) to encode skeleton relative query locations unless paired with direction information in our full model (72 dim, w/o positional encoding).

Position Rep.	Direction Rep.	PSNR ↑	SSIM ↑	#dim for each Rep.
Rel. Dist.	Rel. Ray	20.25	0.8646	360 + 0 + 648
Rel. Dist. + Rotation angles (θ as input)	Rel. Ray	19.25	0.8152	360 + 72 + 648
Rel. Dist. + Rel. Dir. (our full model)	Rel. Ray	24.18	0.9333	360 + 72 + 648

Table 5. Directional encoding impact. The influence of the directional encoding is small but noticeable. It works best to transfer the ray direction relative to the bone coordinates.

Position Rep.	Direction Rep.	PSNR ↑	SSIM ↑	#dim for each Rep.
Rel. Dist. + Rel. Dir.	World Ray Dir.	23.85	0.9304	360 + 72 + 27
Rel. Dist. + Rel. Dir.	Ray Ang.	23.92	0.9318	360 + 72 + 216
Rel. Dist. + Rel. Dir. (our full model)	Rel. Ray	24.18	0.9333	360 + 72 + 648

Table 6. Cutoff influence. Our cutoff limits the influence radius of each bone, thereby increasing accuracy particularly in the foreground (PSNR depicted in braces).

Cutoff Type	Position Rep.	Direction Rep.	PSNR ↑	SSIM ↑
None	Rel. Dist. + Rel. Dir.	Rel. Ray	24.12 (19.50)	0.9228 (0.7803)
Hard	Rel. Dist. + Rel. Dir.	Rel. Ray	24.24 (19.58)	0.9339 (0.7822)
Soft	Rel. Dist. + Rel. Dir.	Rel. Ray	24.18 (19.73)	0.9333 (0.7842)

15), no matter how the directional information of the neural radiance field is encoded (Ray Ang. or Rel. Ray). Our subsequent attempt of positionally encoding a point relatively to every bone of the skeleton (Rel. Pos.) succeeds with a decent PSNR score but has excessive dimensionality and therefore memory consumption (1200 dimensional). Our full final encoding that uses distances and direction is 33% smaller (792 dimensional). Due to the quadratic complexity of MLPs, this leads to a neural network parameter reduction of 23.3% (from 1232900 to 946500) and equal amount of speedup (gradient descent iterations per hour). This experiment was performed without cutoff.

Encoding the query location as the distance to all joint locations, similar to [Moreno-Noguer 2017], has the advantage of a low dimensionality (one distance per joint), which is dramatic because the subsequent positional encoding multiplies the dimensionality. However, Table 4 shows that this leads to reduced visual quality, even when additionally conditioning on the input pose θ . Our full model requires in addition the direction from query to joint in relative bone coordinates (Rel. Dist + Rel. Dir. + Ray Dir.), which attains a 20% higher PSNR while only marginally increasing the memory footprint as Rel. Dir. succeeds without positional encoding.

Impact of View Direction Encoding. The effect of the direction encoding on the radiance field has a smaller influence on the final result since it predominantly models low-frequency shading information. Table 5 reveals that positional encoding of the view-ray direction relative to the bone coordinates works best. It exhibits less artifacts compared to only storing the ray angle.



Fig. 7. **Bullet time effect using A-NeRF.** The camera can be freely rotated and the focal length and position can be changed at test time to synthesize novel views of performances captured with A-NeRF. This example is captured from nine virtual cameras.

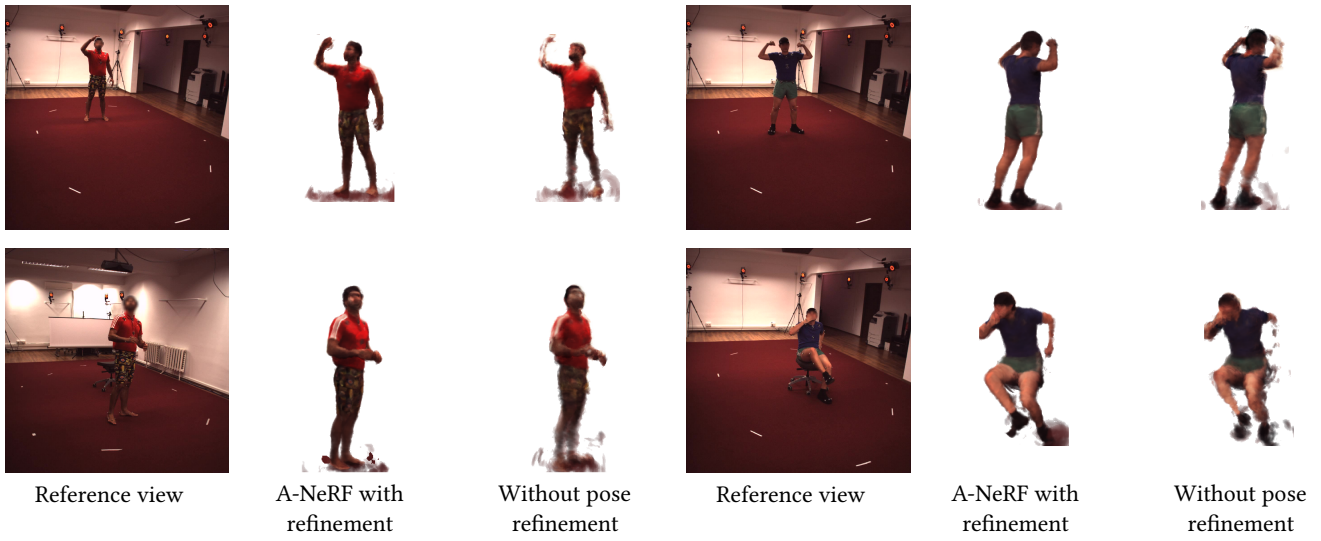


Fig. 8. **Joint optimization and pose refinement** corrects errors in the pose estimation and leads to more accurate A-NeRF models. Texture details improve and noise is drastically reduced as the model better aligns with the input image after pose refinement. Artifacts remain at the intersection of the human body model with objects, such as the floor and a chair (bottom right) since disentanglement without prior shape models is difficult. All results are single-view. Faces in H3.6M images blurred for anonymity.

Impact of Cutoff. Adding the distance-dependent cutoff further boosts the quality, primarily removing ghosting artifacts around the person. Table 6 compares the different variants, soft cutoff (50cm as cutoff threshold) strikes the best compromise between foreground (reported in braces in Table 6) and background metrics. The foreground metrics are computed only over those pixels contained within the ground truth mask, which is known exactly on the synthetic test sequences.

5 APPLICATIONS

We further evaluate our approach in two application scenarios, in addition to the previous quantitative evaluation sequences.

Novel-View Synthesis. Even though our human body models are learned from single camera views, we can synthesize the same pose in a novel view by changing the skeleton position and orientation relative to the camera. This can be used for bullet time effects in movies, for stereoscopic rendering and other entertainment forms,

and as a tool for visualizing motions in 3D for sports and medical analysis by experts. Figure 7 demonstrates a bullet time effect and the teaser, Figure 1, shows two of our characters learned from synthetic data, the female learned from just a single view and the male from multi-view. Irrespective of body shape and number of views, both characters are crisp and nearly indistinguishable from the mesh models they are trained on. Reconstructing real images is considerably more difficult due to motion blur, varying illumination, and limited image resolution. Figure 8 shows our reconstruction from the Human 3.6M test set, rendered from a novel view. While artifacts remain due to 1) shadowing on the floor and objects (chair) that are present in some frames are partially modelled by A-NeRF, 2) color ambiguities between legs and reddish background, and 3) the surface-free volumetric model not perfectly learning all dependencies. Still, the skeleton pose refinement significantly improves results and makes learning from real images possible.

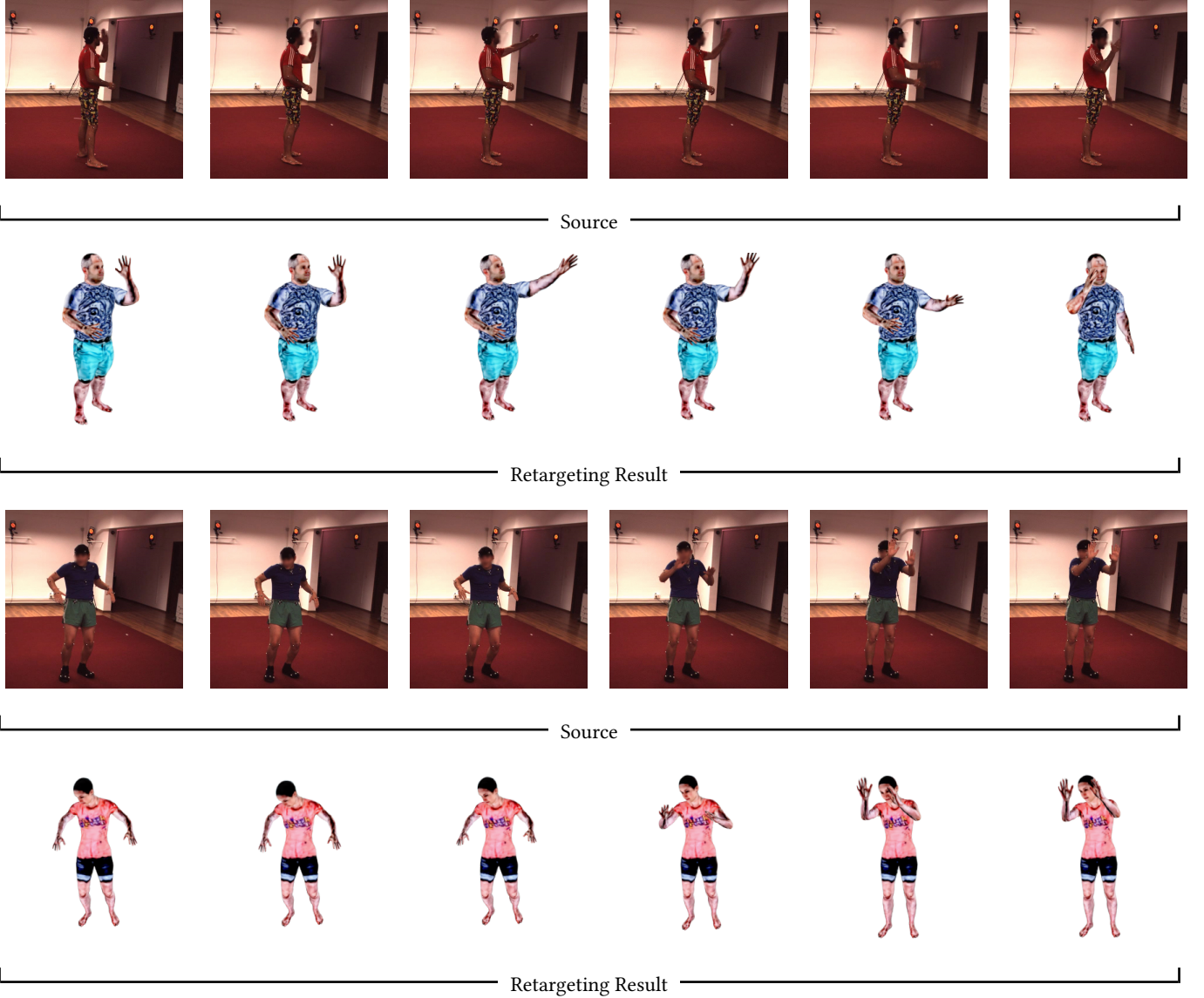


Fig. 9. Motion retargeting from H3.6M reconstructions to SURREAL characters, both reconstructed with A-NeRF. The underlying kinematic skeleton can be posed and animated as a regular rig, here shown with a simple transfer of joint angles over time and rendered from a side view. H3.6M characters are learned from single view. The male SURREAL characters are captured from 9 views and the female from a single one, yet both are of similar quality. Faces in H3.6M images blurred for anonymity.

Motion Retargeting. A classic animation application is the retargeting of a source motion onto a target character. Since we learn a body model and pose simultaneously, A-NeRF can act as a motion source and character source. To demonstrate this, we used continuous videos from the Human3.6M dataset, refined pose with the A-NeRF model optimized on the entire set, and retargeted them onto the SURREAL characters, see Figure 9. Conversely, Figure 10 drives the Human3.6M characters with CMU skeleton motion. This works as long as both characters have the same underlying skeleton by combining the fixed neural network parameters of the target character with the source skeleton pose.

5.1 Discussion, Limitations, and Future Work

The advantage of the neural model is that no explicit volumetric modeling, surface scan, skinning function, and association of points to rigid bones is necessary. These steps are learned end-to-end from image data and apply to diverse motions, shapes, and appearances. Still, the resulting neural body model can be posed by key-framing or motion retargeting. Our learned models are actor specific. It is an interesting future direction to learn a parametric A-NeRF body shape space on a diverse set of actors and apparels, similarly to how surface-based models are currently trained on laser-scans. This

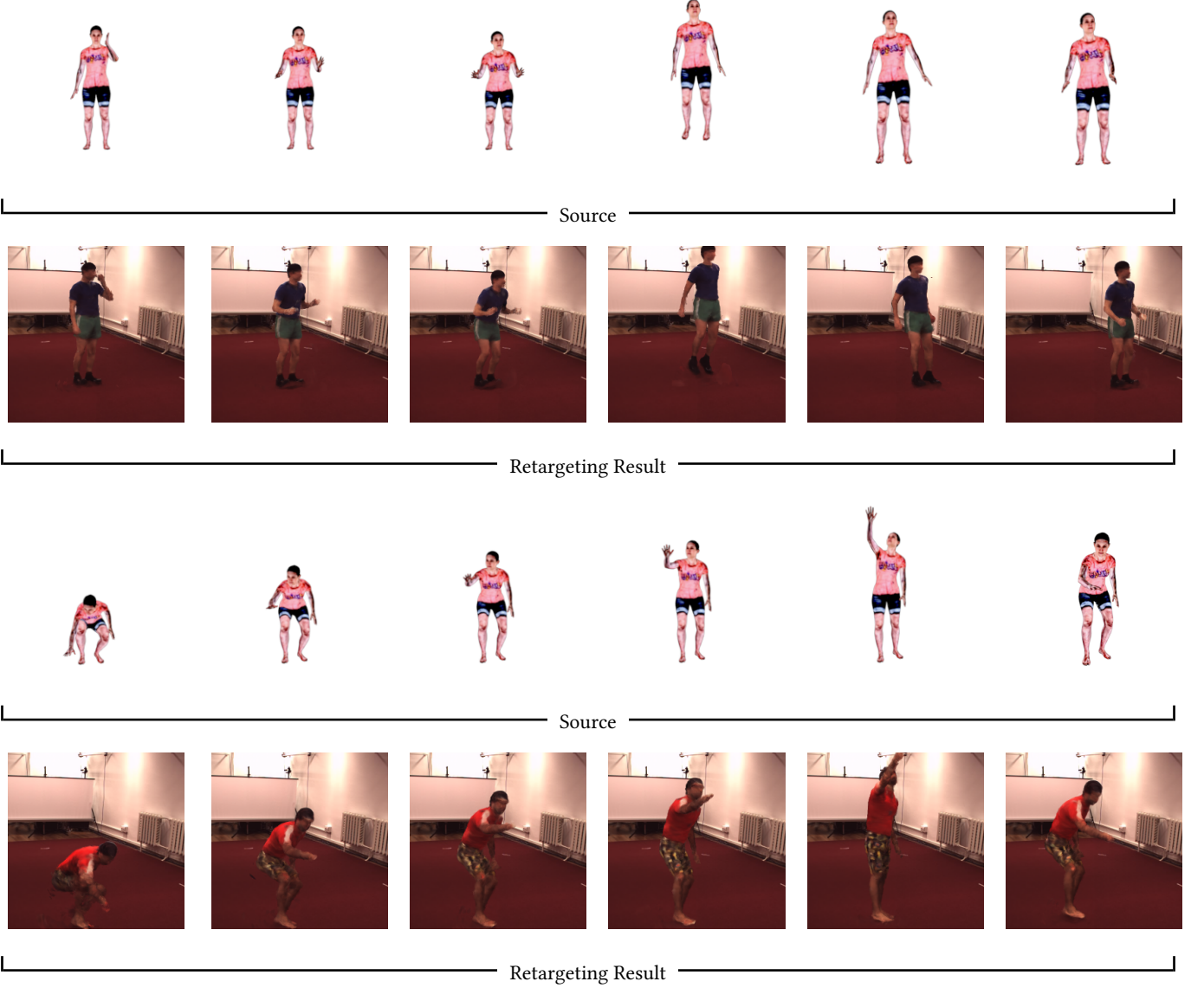


Fig. 10. **Motion retargeting from CMU Mocap sequence to A-NeRF characters** learned using the H3.6M dataset. The transfer works also from existing motion capture data when the underlying skeletons are either matching or can be matched with existing animation pipelines. All depicted characters are learned from single view video footage.

would allow artists to edit shape and appearance in low-dimensional spaces, as for a classical rig.

Our required computation time is enormous and the biggest bottleneck in extending to long sequences and multiple actors. Some of the remaining artifacts can also be attributed to the low number of ray samples we use to make reconstruction and rendering tractable. We believe that the underlying ray-tracing model will benefit from the emerging ray-tracing hardware and can be further improved by optimizations known in the rendering literature.

In contrast to classical analysis-by-synthesis approaches that optimize over a short video and exploit temporal constraints, we found

training on a diverse set of poses sampled uniformly from the available input videos the most effective use of the available resources. Although a single static camera suffices, A-NeRF requires to see the person from all sides in varying poses, to learn pose dependencies and independence. This is in contrast to other works that require as little motion as possible [Alldieck et al. 2018a]. Nevertheless, once a body representation is learned, continuous motion can be reconstructed on consecutive video frames with the volumetric model being fixed.

6 CONCLUSION

We proposed a fully automatic approach for estimating a volumetric actor model and jointly refining skeleton pose from monocular or multi-view video. A-NeRF is the first approach to define NeRF models for extreme and articulated motion and scores high on the Human 3.6 Million benchmark. Based on a new and compact skeleton-relative embedding, our approach reconstructs a personalized volumetric density field with texture detail and time-varying poses of an actor. Importantly, it works from a single video and naturally extends to multi-view, but does not require camera calibration in either of them. This is an important step towards making motion capture more accurate and practical.

6.1 Acknowledgements

Shih-Yang Su, Frank Yu and Helge Rhodin were supported by Compute Canada and Advanced Research Computing at the University of British Columbia [Computing 2019].

REFERENCES

- Kara-Ali Aliev, Artem Sevastopolsky, Maria Kolos, Dmitry Ulyanov, and Victor Lempitsky. 2019. Neural point-based graphics. *arXiv preprint arXiv:1906.08240* (2019).
- Thiemo Alldieck, Marcus Magnor, Bharat Lal Bhatnagar, Christian Theobalt, and Gerard Pons-Moll. 2019a. Learning to reconstruct people in clothing from a single RGB camera. In *CVPR*. 1175–1186.
- Thiemo Alldieck, Marcus Magnor, Weipeng Xu, Christian Theobalt, and Gerard Pons-Moll. 2018a. Detailed human avatars from monocular video. In *2018 International Conference on 3D Vision (3DV)*. IEEE, 98–109.
- T. Alldieck, M. Magnor, W. Xu, C. Theobalt, and G. Pons-moll. 2018b. Video Based Reconstruction of 3D People Models. In *Conference on Computer Vision and Pattern Recognition*.
- Thiemo Alldieck, Gerard Pons-Moll, Christian Theobalt, and Marcus Magnor. 2019b. Tex2Shape: Detailed Full Human Body Geometry From a Single Image. In *Proceedings of the IEEE/CVF International Conference on Computer Vision (ICCV)*.
- Alexandru O Balan, Leonid Sigal, Michael J Black, James E Davis, and Horst W Haussecker. 2007. Detailed human shape and pose from images. In *CVPR*. 1–8.
- Bharat Lal Bhatnagar, Garvita Tiwari, Christian Theobalt, and Gerard Pons-Moll. 2019. Multi-Garment Net: Learning to Dress 3D People from Images. In *IEEE International Conference on Computer Vision (ICCV)*. IEEE.
- Federica Bogo, Angjoo Kanazawa, Christoph Lassner, Peter Gehler, Javier Romero, and Michael J Black. 2016. Keep it SMPL: Automatic estimation of 3D human pose and shape from a single image. In *ECCV*. Springer, 561–578.
- Cristian Sminchisescu Catalin Ionescu, Fuxin Li. 2011. Latent Structured Models for Human Pose Estimation. In *International Conference on Computer Vision*.
- Vasileios Choutas, Georgios Pavlakos, Timo Bolkart, Dimitrios Tzionas, and Michael J. Black. 2020. Monocular Expressive Body Regression through Body-Driven Attention. In *ECCV*. <https://expose.is.tue.mpg.de>
- UBC Advanced Research Computing. 2019. UBC ARC Sockeye. (2019). <https://doi.org/10.14288/SOCKEYE>.
- Boyang Deng, JP Lewis, Timothy Jeruzalski, Gerard Pons-Moll, Geoffrey Hinton, Mohammad Norouzi, and Andrea Tagliasacchi. 2019. NASA: neural articulated shape approximation. *arXiv preprint arXiv:1912.03207* (2019).
- Junting Dong, Qing Shuai, Yuanqing Zhang, Xian Liu, Xiaowei Zhou, and Hujun Bao. 2020. Motion capture from internet videos. In *European Conference on Computer Vision*. Springer, 210–227.
- Yilun Du, Yinan Zhang, Hong-Xing Yu, Joshua B Tenenbaum, and Jiajun Wu. 2020. Neural Radiance Flow for 4D View Synthesis and Video Processing. *arXiv e-prints* (2020), arXiv-2012.
- Guy Gafni, Justus Thies, Michael Zollhöfer, and Matthias Nießner. 2020. Dynamic Neural Radiance Fields for Monocular 4D Facial Avatar Reconstruction. *arXiv preprint arXiv:2012.03065* (2020).
- Chen Gao, Yichang Shih, Wei-Sheng Lai, Chia-Kai Liang, and Jia-Bin Huang. 2020. Portrait Neural Radiance Fields from a Single Image. *arXiv preprint arXiv:2012.05903* (2020).
- Peng Guan, A. Weiss, A. O. Bălan, and M. J. Black. 2009. Estimating human shape and pose from a single image. In *CVPR*. 1381–1388. <https://doi.org/10.1109/ICCV.2009.5459300>
- Riza Alp Guler and Iasonas Kokkinos. 2019. Holopose: Holistic 3d human reconstruction in-the-wild. In *CVPR*. 10884–10894.
- Marc Habermann, Weipeng Xu, , Michael Zollhoefer, Gerard Pons-Moll, and Christian Theobalt. 2019. LiveCap: Real-time Human Performance Capture from Monocular Video. *ACM Transactions on Graphics, (Proc. SIGGRAPH)* (jul 2019).
- Tong He, John Collomosse, Hailin Jin, and Stefano Soatto. 2020. Geo-PIFu: Geometry and Pixel Aligned Implicit Functions for Single-view Human Reconstruction. *arXiv preprint arXiv:2006.08072* (2020).
- Zeng Huang, Yuanlu Xu, Christoph Lassner, Hao Li, and Tony Tung. 2020. ARCH: Animatable Reconstruction of Clothed Humans. In *2020 IEEE/CVF Conference on Computer Vision and Pattern Recognition, CVPR 2020, Seattle, WA, USA, June 13–19, 2020*. IEEE, 3090–3099. <https://doi.org/10.1109/CVPR42600.2020.00316>
- Catalin Ionescu, Dragos Papava, Vlad Olaru, and Cristian Sminchisescu. 2014. Human3.6M: Large Scale Datasets and Predictive Methods for 3D Human Sensing in Natural Environments. *IEEE Transactions on Pattern Analysis and Machine Intelligence* 36, 7 (jul 2014), 1325–1339.
- Karim Iskakov, Egor Burkov, Victor Lempitsky, and Yury Malkov. 2019. Learnable triangulation of human pose. In *ICCV*.
- Arjun Jain, Thorsten Thormählen, Hans-Peter Seidel, and Christian Theobalt. 2010. MovieReshape: Tracking and Reshaping of Humans in Videos. *TOG* 29, 6, Article 148 (Dec. 2010), 10 pages. <https://doi.org/10.1145/1882261.1866174>
- Angjoo Kanazawa, Michael J. Black, David W. Jacobs, and Jitendra Malik. 2018. End-to-end Recovery of Human Shape and Pose. In *CVPR*.
- Diederik P Kingma and Jimmy Ba. 2015. Adam: A method for stochastic optimization. In *ICLR*.
- Muhammed Kocabas, Nikos Athanasiou, and Michael J Black. 2020. VIBE: Video inference for human body pose and shape estimation. In *CVPR*. 5253–5263.
- Nikos Kolotouros, Georgios Pavlakos, Michael J Black, and Kostas Daniilidis. 2019. Learning to reconstruct 3D human pose and shape via model-fitting in the loop. In *ICCV*. 2252–2261.
- Christoph Lassner, Javier Romero, Martin Kiefel, Federica Bogo, Michael J. Black, and Peter V. Gehler. 2017. Unite the People: Closing the Loop Between 3D and 2D Human Representations. In *CVPR*.
- Christoph Lassner and Michael Zollhöfer. 2020. Pulsar: Efficient Sphere-based Neural Rendering. *arXiv:2004.07484 [cs.GR]*
- Shichao Li, Lei Ke, Kevin Pratama, Yu-Wing Tai, Chi-Keung Tang, and Kwang-Ting Cheng. 2020a. Cascaded Deep Monocular 3D Human Pose Estimation With Evolutionary Training Data. In *Proceedings of the IEEE/CVF Conference on Computer Vision and Pattern Recognition (CVPR)*.
- Zhengqi Li, Simon Niklaus, Noah Snavely, and Oliver Wang. 2020b. Neural Scene Flow Fields for Space-Time View Synthesis of Dynamic Scenes. *arXiv preprint arXiv:2011.13084* (2020).
- Lingjie Liu, Jiatao Gu, Kyaw Zaw Lin, Tat-Seng Chua, and Christian Theobalt. 2020. Neural sparse voxel fields. *NeurIPS* 33 (2020).
- Shichen Liu, Tianye Li, Weikai Chen, and Hao Li. 2019. Soft rasterizer: A differentiable renderer for image-based 3d reasoning. In *Proceedings of the IEEE/CVF International Conference on Computer Vision*. 7708–7717.
- Stephen Lombardi, Jason Saragih, Tomas Simon, and Yaser Sheikh. 2018. Deep Appearance Models for Face Rendering. *ACM Trans. Graph.* 37, 4, Article 68 (July 2018), 13 pages. <https://doi.org/10.1145/3197517.3201401>
- Stephen Lombardi, Tomas Simon, Jason Saragih, Gabriel Schwartz, Andreas Lehrmann, and Yaser Sheikh. 2019. Neural Volumes: Learning Dynamic Renderable Volumes from Images. *ACM Trans. Graph.* 38, 4, Article 65 (July 2019), 14 pages. <https://doi.org/10.1145/3306346.3323020>
- Matthew Loper, Naureen Mahmood, Javier Romero, Gerard Pons-Moll, and Michael J Black. 2015. SMPL: A skinned multi-person linear model. *ACM TOG (Proc. SIGGRAPH)* 34, 6 (2015), 1–16.
- Ricardo Martin-Brualla, Noha Radwan, Mehdi SM Sajjadi, Jonathan T Barron, Alexey Dosovitskiy, and Daniel Duckworth. 2020. Nerf in the wild: Neural radiance fields for unconstrained photo collections. *arXiv preprint arXiv:2008.02268* (2020).
- Julietta Martinez, Rayat Hossain, Javier Romero, and James J Little. 2017. A simple yet effective baseline for 3d human pose estimation. In *ICCV*.
- Dushyanth Mehta, Oleksandr Sotnychenko, Franziska Mueller, Weipeng Xu, Mohamed Elgharib, Pascal Fuat, Hans-Peter Seidel, Helge Rhodin, Gerard Pons-Moll, and Christian Theobalt. 2020. XNect: Real-time Multi-Person 3D Motion Capture with a Single RGB Camera. *ACM Transactions on Graphics* 39, 4, 17. <https://doi.org/10.1145/3386569.3392410>
- Dushyanth Mehta, Srinath Sridhar, Oleksandr Sotnychenko, Helge Rhodin, Mohammad Shafiei, Hans-Peter Seidel, Weipeng Xu, Dan Casas, and Christian Theobalt. 2017. VNect: Real-time 3D Human Pose Estimation with a Single RGB Camera. In *TOG*, Vol. 36. 14. <https://doi.org/10.1145/3072959.3073596>
- Moustafa Meshry, Dan B Goldman, Sameh Khamis, Hugues Hoppe, Rohit Pandey, Noah Snavely, and Ricardo Martin-Brualla. 2019. Neural rerendering in the wild. In *Proceedings of the IEEE Conference on Computer Vision and Pattern Recognition*. 6878–6887.
- Ben Mildenhall, Pratul P Srinivasan, Matthew Tancik, Jonathan T Barron, Ravi Ramamoorthi, and Ren Ng. 2020. NeRF: Representing Scenes as Neural Radiance Fields for View Synthesis. In *ECCV*.

- Francesc Moreno-Noguer. 2017. 3D Human Pose Estimation from a Single Image via Distance Matrix Regression, In Proceedings of the Conference on Computer Vision and Pattern Recognition (CVPR). *Conference on Computer Vision and Pattern Recognition (CVPR)*.
- Aiden Nibali, Zhen He, Stuart Morgan, and Luke Prendergast. 2019. 3d human pose estimation with 2d marginal heatmaps. In *WACV*.
- Mohamed Omran, Christof Lassner, Gerard Pons-Moll, Peter Gehler, and Bernt Schiele. 2018. Neural Body Fitting: Unifying Deep Learning and Model Based Human Pose and Shape Estimation. In *3DV*.
- Sergio Orts-Escalante, Christoph Rhemann, Sean Fanello, Wayne Chang, Adarsh Kowdle, Yury Degtyarev, David Kim, Philip L. Davidson, Sameh Khamis, Mingsong Dou, Vladimir Tankovich, Charles Loop, Qin Cai, Philip A. Chou, Sarah Mennicken, Julien Valentin, Vivek Pradeep, Shenlong Wang, Sing Bing Kang, Pushmeet Kohli, Yuliya Lutchny, Cem Keskin, and Shahram Izadi. 2016. Holoportation: Virtual 3D Teleportation in Real-Time. In *Proceedings of the 29th Annual Symposium on User Interface Software and Technology* (Tokyo, Japan) (*UIST ’16*). Association for Computing Machinery, New York, NY, USA, 741–754. <https://doi.org/10.1145/2984511.2984517>
- Keunhong Park, Utkarsh Sinha, Jonathan T Barron, Sofien Bouaziz, Dan B Goldman, Steven M Seitz, and Ricardo-Martin Bralla. 2020. Deformable Neural Radiance Fields. *arXiv preprint arXiv:2011.12948* (2020).
- Georgios Pavlakos, Xiaowei Zhou, Konstantinos G Derpanis, and Kostas Daniilidis. 2017. Coarse-to-fine volumetric prediction for single-image 3D human pose. In *CVPR*.
- Georgios Pavlakos, Luyang Zhu, Xiaowei Zhou, and Kostas Daniilidis. 2018. Learning to Estimate 3D Human Pose and Shape from a Single Color Image. In *CVPR*.
- Sida Peng, Yuanqing Zhang, Yinghao Xu, Qianqian Wang, Qing Shuai, Hujun Bao, and Xiaowei Zhou. 2020. Neural Body: Implicit Neural Representations with Structured Latent Codes for Novel View Synthesis of Dynamic Humans. *arXiv preprint arXiv:2012.15838* (2020).
- Albert Pumarola, Enric Corona, Gerard Pons-Moll, and Francesc Moreno-Noguer. 2020. D-NeRF: Neural Radiance Fields for Dynamic Scenes. *arXiv preprint arXiv:2011.13961* (2020).
- Helge Rhodin, Christian Richardt, Dan Casas, Eldar Insafutdinov, Mohammad Shafiei, Hans-Peter Seidel, Bernt Schiele, and Christian Theobalt. 2016a. Egocap: egocentric marker-less motion capture with two fisheye cameras. *ACM Transactions on Graphics (TOG)* 35, 6 (2016), 1–11.
- Helge Rhodin, Nadia Robertini, Dan Casas, Christian Richardt, Hans-Peter Seidel, and Christian Theobalt. 2016b. General automatic human shape and motion capture using volumetric contour cues. In *ECCV*. 509–526.
- Helge Rhodin, Nadia Robertini, Christian Richardt, Hans-Peter Seidel, and Christian Theobalt. 2015. A versatile scene model with differentiable visibility applied to generative pose estimation. In *ICCV*. 765–773.
- Nadia Robertini, Dan Casas, Helge Rhodin, Hans-Peter Seidel, and Christian Theobalt. 2016. Model-based outdoor performance capture. In *2016 Fourth International Conference on 3D Vision (3DV)*. IEEE, 166–175.
- Shunsuke Saito, Zeng Huang, Ryota Natsume, Shigeo Morishima, Angjoo Kanazawa, and Hao Li. 2019. Pifu: Pixel-aligned implicit function for high-resolution clothed human digitization. In *CVPR*. 2304–2314.
- Shunsuke Saito, Tomas Simon, Jason Saragih, and Hanbyul Joo. 2020. PIFuHD: Multi-Level Pixel-Aligned Implicit Function for High-Resolution 3D Human Digitization. In *CVPR*. 84–93.
- Katja Schwarz, Yiyi Liao, Michael Niemeyer, and Andreas Geiger. 2020. Graf: Generative radiance fields for 3d-aware image synthesis. *NeurIPS* 33 (2020).
- Mingyi Shi, Kfir Aberman, Andreas Aristidou, Taku Komura, Dani Lischinski, Daniel Cohen-Or, and Baoquan Chen. 2020. MotioNet: 3D Human Motion Reconstruction from Monocular Video with Skeleton Consistency. *ACM Transactions on Graphics (TOG)* 40, 1 (2020), 1–15.
- Vincent Sitzmann, Julien Martel, Alexander Bergman, David Lindell, and Gordon Wetzstein. 2020. Implicit neural representations with periodic activation functions. *NeurIPS* 33 (2020).
- V. Sitzmann, J. Thies, F. Heide, M. Nießner, G. Wetzstein, and M. Zollhöfer. 2019a. DeepVoxels: Learning Persistent 3D Feature Embeddings. In *Proceedings of Computer Vision and Pattern Recognition (CVPR 2019)*.
- Vincent Sitzmann, Michael Zollhöfer, and Gordon Wetzstein. 2019b. Scene representation networks: Continuous 3d-structure-aware neural scene representations. In *Advances in Neural Information Processing Systems*. 1121–1132.
- Carsten Stoll, Nils Hasler, Juergen Gall, Hans-Peter Seidel, and Christian Theobalt. 2011. Fast articulated motion tracking using a sum of Gaussians body model. In *ICCV*. 951–958.
- Matthew Tancik, Pratul P Srinivasan, Ben Mildenhall, Sara Fridovich-Keil, Nithin Raghavan, Utkarsh Singh, Ravi Ramamoorthi, Jonathan T Barron, and Ren Ng. 2020. Fourier Features Let Networks Learn High Frequency Functions in Low Dimensional Domains. *NeurIPS* (2020).
- Jonathan Taylor, Jamie Shotton, Toby Sharp, and Andrew Fitzgibbon. 2012. The vitruvian manifold: Inferring dense correspondences for one-shot human pose estimation. In *CVPR* IEEE, 103–110.
- A. Tewari, O. Fried, J. Thies, V. Sitzmann, S. Lombardi, K. Sunkavalli, R. Martin-Brualla, T. Simon, J. Saragih, M. Nießner, R. Pandey, S. Fanello, G. Wetzstein, J.-Y. Zhu, C. Theobalt, M. Agrawala, E. Shechtman, D. B Goldman, and M. Zollhöfer. 2020. State of the Art on Neural Rendering. *Computer Graphics Forum (EG STAR 2020)* (2020).
- Justus Thies, Michael Zollhöfer, and Matthias Nießner. 2019. Deferred Neural Rendering: Image Synthesis using Neural Textures. *ACM Transactions on Graphics 2019 (TOG)* (2019).
- Denis Tome, Matteo Toso, Lourdes Agapito, and Chris Russell. 2018. Rethinking pose in 3d: Multi-stage refinement and recovery for markerless motion capture. In *3DV*. IEEE.
- Edgar Treitschke, Ayush Tewari, Vladislav Golyanik, Michael Zollhöfer, Christoph Lassner, and Christian Theobalt. 2020. Non-Rigid Neural Radiance Fields: Reconstruction and Novel View Synthesis of a Deforming Scene from Monocular Video. *arXiv preprint arXiv:2012.12247* (2020).
- Alex Trevithick and Bo Yang. 2020. GRF: Learning a General Radiance Field for 3D Scene Representation and Rendering. *arXiv preprint arXiv:2010.04595* (2020).
- Hsiao-Yu Tung, Hsiao-Wei Tung, Ersin Yumer, and Katerina Fragkiadaki. 2017. Self-supervised Learning of Motion Capture. In *NeurIPS*. 5242–5252.
- Gül Varol, Javier Romero, Xavier Martin, Naureen Mahmood, Michael J. Black, Ivan Laptev, and Cordelia Schmid. 2017. Learning from Synthetic Humans. In *CVPR*.
- Ashish Vaswani, Noam Shazeer, Niki Parmar, Jakob Uszkoreit, Llion Jones, Aidan N Gomez, Łukasz Kaiser, and Illia Polosukhin. 2017. Attention is all you need. In *NeurIPS*.
- Zhou Wang, Alan C Bovik, Hamid R Sheikh, and Eero P Simoncelli. 2004. Image quality assessment: from error visibility to structural similarity. *IEEE transactions on image processing* 13, 4 (2004), 600–612.
- Olivia Wiles, Georgia Gkioxari, Richard Szeliski, and Justin Johnson. 2020. Synsin: End-to-end view synthesis from a single image. In *Proceedings of the IEEE/CVF Conference on Computer Vision and Pattern Recognition*. 7467–7477.
- Chenglei Wu, Kiran Varanasi, Yebin Liu, Hans-Peter Seidel, and Christian Theobalt. 2011. Shading-based dynamic shape refinement from multi-view video under general illumination. In *IEEE International Conference on Computer Vision, ICCV 2011, Barcelona, Spain, November 6–13, 2011*, Dimitris N. Metaxas, Long Quan, Alberto Sanfelix, and Luc Van Gool (Eds.). IEEE Computer Society, 1108–1115. <https://doi.org/10.1109/ICCV.2011.6126358>
- Wenqi Xian, Jia-Bin Huang, Johannes Kopf, and Changil Kim. 2020. Space-time Neural Irradiance Fields for Free-Viewpoint Video. *arXiv preprint arXiv:2011.12950* (2020).
- Donglai Xiang, Hanbyul Joo, and Yaser Sheikh. 2019. Monocular total capture: Posing face, body, and hands in the wild. In *Proceedings of the IEEE/CVF Conference on Computer Vision and Pattern Recognition*. 10965–10974.
- Jingwei Xu, Zhenbo Yu, Bingbing Ni, Jiancheng Yang, Xiaokang Yang, and Wenjun Zhang. 2020. Deep Kinematics Analysis for Monocular 3D Human Pose Estimation. In *Proceedings of the IEEE/CVF Conference on Computer Vision and Pattern Recognition (CVPR)*.
- Weipeng Xu, Avishek Chatterjee, Michael Zollhöfer, Helge Rhodin, Dushyant Mehta, Hans-Peter Seidel, and Christian Theobalt. 2018. Monoperfcap: Human performance capture from monocular video. *TOG* 37, 2 (2018), 27.
- Alex Yu, Vickie Ye, Matthew Tancik, and Angjoo Kanazawa. 2020. pixelNeRF: Neural Radiance Fields from One or Few Images. *arXiv preprint arXiv:2012.02190* (2020).
- Kai Zhang, Gernot Riegler, Noah Snavely, and Vladlen Koltun. 2020. Nerf++: Analyzing and improving neural radiance fields. *arXiv preprint arXiv:2010.07492* (2020).
- Xingyi Zhou, Xiao Sun, Wei Zhang, Shuang Liang, and Yichen Wei. 2016. Deep Kinematic Pose Regression. In *ECCV Workshop*.
- Yi Zhou, Connelly Barnes, Jingwan Lu, Jimei Yang, and Hao Li. 2019. On the continuity of rotation representations in neural networks. In *Proceedings of the IEEE/CVF Conference on Computer Vision and Pattern Recognition*. 5745–5753.
- Silvia Zuffi, Angjoo Kanazawa, Tanya Berger-Wolf, and Michael J. Black. 2019. Three-D Safari: Learning to Estimate Zebra Pose, Shape, and Texture from Images "In the Wild". In *International Conference on Computer Vision*. IEEE, 5358–5367.